Type-I clathrate calcium hydride and its hydrogen-vacancy structures at high pressure

Decheng An,[1] Defang Duan,[1,*] Zihan Zhang,[1] Qiwen Jiang,[1] Tiancheng Ma,[1] Zihao Huo,[1] Hao Song,[2] and Tian Cui[1,2,†]

[1]*State Key Laboratory of Superhard Materials and Key Laboratory of Material Simulation Methods and Software of Ministry of Education, College of Physics, Jilin University, Changchun 130012, China*

[2]*Institute of High Pressure Physics, School of Physical Science and Technology, Ningbo University, Ningbo 315211, China*

(Received 7 February 2024; revised 17 July 2024; accepted 19 July 2024; published 6 August 2024)

Recently, the first predicted metal clathrate hydride CaH_6 was successfully synthesized experimentally and shown to have a superconducting critical temperature T_c exceeding 200 K. However, experimental findings suggest the existence of additional unidentified phases besides CaH_6. In this study, we performed an extensive structure search of the Ca–H system at 200 GPa, revealing a thermodynamically stable type-I clathrate hydride, Ca_8H_{46}, along with two analogous structures featuring hydrogen vacancies. Ca_8H_{46} exhibits a high T_c range of 210–223 K at 150 GPa, and the presence of hydrogen vacancies shifts the T_c. Our simulated x-ray-diffraction patterns, calculated equation of state, and T_c's for Ca_8H_x ($x = 44-46$) agree with the experimental results, confirming their presence in multiple synthesized phases. Our findings serve to revise the Ca–H phase diagram under high pressure and offer valuable insights into the effects of hydrogen vacancies in Ca_8H_{46}, which explain the anomalous decrease in T_c observed in experiments.

DOI: 10.1103/PhysRevB.110.054505

I. INTRODUCTION

Research on superconductivity in superhydrides has gained significant attention following the successful prediction and synthesis of the covalent hydride H_3S, which exhibits a T_c of 203 K at 155 GPa [1–3]. This achievement has inspired extensive research efforts aimed at achieving high- and room-temperature superconductivity in superhydrides or other light-element compounds [4–7]. Subsequent predictions and high-pressure experiments have also confirmed the presence of high-temperature superconductivity in some hydride systems [8–14], such as La–H, Y–H, and Ca–H. For synthesis of superhydrides in diamond-anvil cell (DAC) experiments, it is extremely difficult to obtain a homogeneous sample because of the limitations of the experimental conditions. Notably, experimental results, including measured T_c values and x-ray-diffraction (XRD) patterns, have suggested the existence of multiple phases in the high-temperature and high-pressure synthesis of some hydrides [13–15]. The presence of multiple phases presents a significant challenge in identifying the superconducting phase and understanding the underlying superconducting mechanisms. For the La–H system, the presence of seven distinct lanthanum hydrides has been identified: LaH_3, $LaH_{\sim 4}$, $LaH_{4+\delta}$, La_4H_{23}, $LaH_{6+\delta}$, $LaH_{9+\delta}$, and $LaH_{10+\delta}$ [15].

For the Ca–H system, besides the known stoichiometric CaH_2, several novel stoichiometric compounds that are thermodynamically stable have been predicted under high pressure, such as CaH, CaH_4, CaH_6, CaH_9, CaH_{12}, and CaH_{15} [10,16–19]. As the first proposed metal clathrate hydride, $Im\bar{3}$ m-CaH_6 was anticipated to exhibit a high T_c of 235 K at 150 GPa [10]. Owing to its novel crystal structure and outstanding superconducting properties, researchers have been actively pursuing the experimental synthesis of CaH_6. Previous experiments have attempted to synthesize CaH_6 by compressing a mixture of Ca and H_2 gas into DACs [20,21]. However, the synthesized calcium hydride was Ca_2H_5 or CaH_4 with low hydrogen content, not CaH_6. After a decade of exploration, CaH_6 was successfully synthesized by replacing H_2 gas with ammonia borane (NH_3BH_3) using DAC combined with an *in situ* laser-heating technique, and the measured maximum superconducting T_c was greater than 210 K [13,14]. Notably, the experimental XRD patterns in two cells (cell_2 and cell_3) reported by Ma *et al.* [13] and XRD patterns reported by Li *et al.* [14] revealed numerous peaks beyond CaH_6, which were unknown and could not be indexed by previously predicted structures. In addition, the temperature-dependent resistance curves exhibited several distinct steps [14]. Finally, it was anomalous that the T_c values dropped quickly with decreasing pressure, which could not be explained only using CaH_6 [13]. These observations collectively suggest the existence of multiple calcium hydride phases. Therefore, further detailed search of the crystal structures and characterization of the superconductivity of the Ca–H system under high pressure are required.

In this paper, we report several unexpected thermodynamically stable stoichiometries, including CaH_{24} and Ca_8H_{46} and its vacancy structures, Ca_8H_{45} and Ca_8H_{44}. The estimated T_c of Ca_8H_{46} reaches 223 K at 150 GPa, and as hydrogen vacancies are introduced, the T_c reduces to 163 K for Ca_8H_{45} and 40 K for Ca_8H_{44}. In a comparison of experimental XRD patterns, equation of state (EOS), and T_c's with theoretically calculated results, Ca_8H_{46} is identified within the multiple phases synthesized experimentally. The

*Contact author: duandf@jlu.edu.cn
†Contact author: cuitian@nbu.edu.cn

impact of hydrogen vacancies on the T_c explains the observed anomalous phenomenon of a rapid decrease in T_c with decreasing pressure. This paper reveals phases not indicated by experimental results and provides a valuable reference for discussing the impacts of hydrogen vacancies on clathrate hydrides.

II. COMPUTATION METHODS

Various composition structure searches for the binary Ca_xH_y system [$x = 1$, $y = 1$ and 21–30; $x = 2-3$, $y = 1-29$, and y:$x \neq$ integer; $x = 4$, y = 1–39, and $y \neq 2n$ (n = integer)] were performed with the AIRSS code at 200 GPa [22]. The stoichiometries Ca_xH_y ($x + y < 15$ and $x = 1$, 2) were performed with simulation cell of 1–4 f.u. (formula units) and the others with simulation cell of 1–2 f.u.. High-accuracy structural relaxations were performed using the VASP code with the projector-augmented wave method [23]. Based on the generalized gradient approximation, the Perdew-Burke-Ernzerhof functional was used as the exchange-correlation functional [24]. For H and Ca, $1s^1$ and $3s^2\,3p^6\,4s^2$ as the valence electrons were choice. The cutoff energy was set to 600 eV with a k-point spacing of $2\pi \times 0.03$ Å^{-1} and $2\pi \times 0.02$ Å^{-1} for the structural relaxations and electronic property calculations, respectively. The choice of cutoff energy and k-point spacing ensured that the enthalpy calculations converged to within 1 meV per atom. Analyses of the diffraction patterns and Rietveld refinements were performed using the GSAS and EXPGUI packages [25].

Phonon-dispersion and electron-phonon coupling (EPC) calculations were performed using the density-functional perturbation theory in the QUANTUM ESPRESSO package [26]. The ultrasoft pseudopotentials [27] and a 70-Ry cutoff energy were chosen for Ca_8H_{46}, Ca_8H_{45}, and Ca_8H_{44}. A $3 \times 3 \times 3$ q mesh and a $12 \times 12 \times 12$ k mesh were adopted for Ca_8H_{46} and Ca_8H_{44}, respectively. A $2 \times 2 \times 2$ q mesh and an $8 \times 8 \times 8$ k mesh were adopted for Ca_8H_{45}. A Methfessel-Paxton first-order smearing of 0.04 Ry and Gaussian width of 0.005 Ry was employed. T_c's were calculated using the Allen-Dynes modified McMillan equation [28] and Eliashberg equation [29–31].

For the Allen-Dynes modified McMillan equation,

$$T_c = \frac{f_1 f_2 \omega_{\log}}{1.2} \exp\left[-\frac{1.04(1+\lambda)}{\lambda - \mu^*(1+0.62\lambda)}\right], \tag{1}$$

where f_1 and f_2, two separate correction factors, are expressed by

$$f_1 = \sqrt[3]{\left[1 + \left(\frac{\lambda}{2.46(1+3.8\mu^*)}\right)^{3/2}\right]}, \tag{2}$$

$$f_2 = 1 + \frac{\left(\frac{\bar{\omega}_2}{\omega_{\log}} - 1\right)\lambda^2}{\lambda^2 + \left[1.82(1+6.3\mu^*)\frac{\bar{\omega}_2}{\omega_{\log}}\right]^2}, \tag{3}$$

where λ, μ^*, $\bar{\omega}_2$, and $\omega_{\log}$ are EPC parameter, Coulomb pseudopotential, mean-square frequency, and logarithmic average frequency, respectively. μ^* is typically used in the range of 0.1-0.13 in hydrides, which could provide a valuable T_c; λ, $\bar{\omega}_2$, and $\omega_{\log}$ were given by

$$\lambda = 2\int \frac{\alpha^2 F(\omega)}{\omega} d\omega, \tag{4}$$

$$\bar{\omega}_2 = \sqrt{\frac{2}{\lambda}\int \alpha^2 F(\omega)\omega d\omega}, \tag{5}$$

$$\omega_{\log} = \exp\left[\frac{2}{\lambda}\int \frac{d\omega}{\omega}\alpha^2 F(\omega)\ln\omega\right]. \tag{6}$$

For the Eliashberg equation,

$$Z(i\omega_j) = 1 + \frac{\pi T}{\omega_j}\sum_{j'} \frac{\omega_{j'}}{\sqrt{\omega_{j'}^2 + \Delta^2(i\omega_{j'})}}\lambda(i\omega_j - i\omega_{j'}), \tag{7}$$

$$Z(i\omega_j)\Delta(i\omega_j) = \pi T \sum_{j'} \frac{\Delta(i\omega_{j'})}{\sqrt{\omega_{j'}^2 + \Delta^2(i\omega_{j'})}} \times [\lambda(i\omega_j - i\omega_{j'}) - \mu^*], \tag{8}$$

$$\lambda(i\omega_j - i\omega_{j'}) = \int d\omega \frac{2\omega\alpha^2 F(\omega)}{\omega^2 + (\omega_j - \omega_{j'})^2}. \tag{9}$$

The T_c is determined as the asymptotic value when $\Delta(i\omega_j)$ approaches zero.

III. RESULTS AND DISCUSSION

We performed an extensive structure search of the Ca–H system at 200 GPa to assess the thermodynamic stability of the calcium hydrides. In addition to the previously reported calcium hydrides, we realized several unexpected stoichiometries: Ca_8H_{44} (Ca_2H_{11}), Ca_8H_{46} (Ca_4H_{23}), and CaH_{24}. We were surprised to find that Ca_8H_{44} can be considered as Ca_8H_{46} with two H vacancies. Hence, we proceeded to generate hydrogen-vacancy structures with single hydrogen vacancy starting from the ideal structure Ca_8H_{46} and obtained a thermodynamically stable Ca_8H_{45} phase. We constructed the convex hull of the Ca–H system at 200 GPa to assess the thermodynamical stability of the calcium hydrides (Fig. 1). Remarkably, the hydrogen-vacancy structures, Ca_8H_{45} and Ca_8H_{44}, as well as the ideal crystal structure, Ca_8H_{46}, can coexist at 200 GPa as thermodynamically stable phases, suggesting the possibility of their simultaneous synthesis. The previously reported thermodynamically stable CaH, CaH_2, and CaH_4 still lie on the convex hull, but CaH_6, CaH_9, CaH_{12}, and CaH_{15} lie above the convex hull and are metastable phases [10,17,18], in which $Im\bar{3}m$-CaH_6 is approximately 22 meV per atom above the convex hull. Furthermore, we performed a comprehensive structure search for Ca_8H_{44}, Ca_8H_{45}, and Ca_8H_{46} at 170, 150, and 130 GPa and construct the thermodynamical convex hull, as shown in Fig. S1 of the Supplemental Material (SM) [32]. The results show that Ca_8H_{44} is still stable in the pressure range of 130–170 GPa. Ca_8H_{45} and Ca_8H_{46} remain stable at 170 and 150 GPa, while both become metastable at 130 GPa, with the enthalpy 2 and 3 meV per atom above the convex hull, respectively. We note that during the preparation of our paper, Ca_8H_{46} was predicted by Sun *et al.* [33]. However, their work focused on a two-step approach based on chemical template

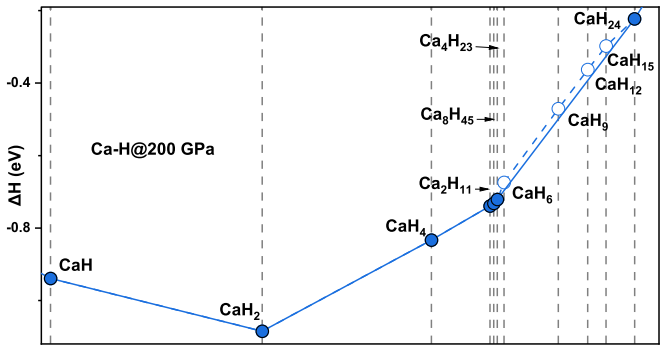

FIG. 1. Enthalpies of formation of predicted Ca–H system relative to *I*4/*mcm*–Ca [35] and *C*2/*c*–H [36] at 200 GPa. Blue-solid and -empty circles represent thermodynamically stable and metastable phases, respectively.

theory [34] and its application, with little discussion of properties.

Ca_8H_{46} adopts the high-symmetry $Pm\bar{3}n$, which represents a type-I clathrate structure, analogous to those observed in metal silicides, such as Na_8Si_{46} [37]. This structure shares its geometry with the Weaire-Phelan structure [38] as an optimal solution to the Kelvin problem, which seeks an efficient arrangement of closely packed units that minimizes surface area while maintaining equal volumes. In $Pm\bar{3}n$-Ca_8H_{46}, Ca atoms occupy the A15 arrangements, and hydrogen atoms participate in the formation of two distinct types of cage basic blocks: the pentagonal dodecahedron formed by 20 hydrogen atoms comprising 12 pentagonal faces, and tetrakaidecahedron formed by 24 hydrogen atoms comprising 12 pentagonal faces and 2 hexagonal faces. H_{20} cages occupy the center and vertices of the cube, whereas H_{24} cages are situated on the faces [Fig. 2(a)]. With the introduction of one and two hydrogen vacancies occupying the 16*i* sites within the cubic lattice of Ca_8H_{46}, these polyhedra begin to deform, resulting in the formation of Ca_8H_{45} and Ca_8H_{44} (Fig. 2). The lattice angles transform from 90 ° to 90.33 ° and 90.37 ° for Ca_8H_{45} and Ca_8H_{44}, respectively.

To confirm our predicted type-I clathrate Ca_8H_{46} and its hydrogen-vacancy structures, we simulated their XRD patterns and compared them with their experimental counterparts. The results show that these three structures have similar peak positions due to their structural similarity, although their peak widths are slightly different (Fig. S2). Simultaneously, we also chose the known structures of $Im\bar{3}$ *m*-CaH_6, *I*4/*mmm*-CaH_4, *P*6/*mmm*-CaH_2, and $Pm\bar{3}$ *m*-CaH to fit the experimental XRD patterns at 173 GPa measured by Ma *et al.* [13] [Fig. 3(a)]. The fitting results show that, except for two peaks at $2\theta = 13.21$ ° and 14.10 °, all Bragg peaks can be indexed to $Pm\bar{3}n$-Ca_8H_{46}, $Im\bar{3}$ *m*-CaH_6, *I*4/*mmm*-CaH_4, *P*6/*mmm*-CaH_2, and $Pm\bar{3}$ *m*-CaH. These results suggest the existence of multiple phases under this synthesis condition, which is consistent with the results of the energetic analysis. Notably, the previously unexplained peaks at $2\theta = 12.94$ °, 14.50 °, and 15.88 ° in the experimental XRD patterns match well with the simulated peak positions of $Pm\bar{3}$ *n*-Ca_8H_{46} [Fig. 3(a)]. The two peaks could not be indexed, indicating the possibility of other calcium hydrides with more complex hydrogen contents.

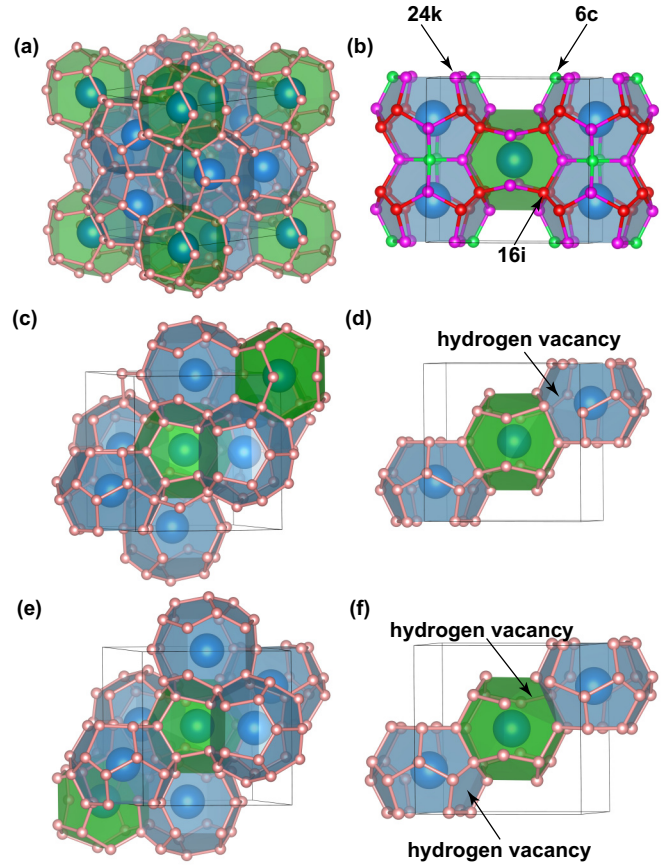

FIG. 2. Crystal structures of (a) $Pm\bar{3}n$-Ca_8H_{46}, (c) *R*3-Ca_8H_{45}, and (e) *R*3c-Ca_8H_{44}. (b) H atom sites in $Pm\bar{3}n$-Ca_8H_{46}, where green, red, and purple spheres represent the 6*c*, 16*i*, and 24*k* Wyckoff sites, respectively. The hydrogen-vacancy positions in (d) *R*3-Ca_8H_{45} and (f) *R*3c-Ca_8H_{44} are indicated by arrows.

The x-ray cross section for hydrogen atoms is notably weak, making it impossible to precisely determine the occupancy details of hydrogen atoms. Unit-cell volume fitting is an available method for determining the stoichiometry of hydrides. We selected the XRD spectra containing three obvious indexed peaks of Ca_8H_{46} under five pressures from cell_3 (Fig. S2) reported by Ma *et al.* [13] to fit its volume, as shown in the orange empty stars of Fig. 3(b). The refined lattice parameter and volume of Ca_8H_{46}, respectively, are 5.457 and 162.50 $Å^3$ at 173 GPa, which closely aligns with our theoretical prediction results of 5.449 and 161.79 $Å^3$. Analysis of both the simulated XRD and calculated EOS suggests the presence of $Pm\bar{3}$ *n*-Ca_8H_{46} in the multiple synthesized phases.

To examine the potential superconductivity of the predicted Ca_8H_{46}, Ca_8H_{45}, and Ca_8H_{44}, we calculated the EPC parameter λ, logarithmic average phonon frequency $\omega_{\log}$, and electronic density of states N (E_f) at the Fermi level. We estimated T_c's based on the Allen-Dynes modified McMillan equation and the Eliashberg equation with a typical Coulomb pseudopotential parameter μ^*, within 0.1–0.13. The results are shown in Table I. The Eliashberg results show that Ca_8H_{46} exhibits a T_c of 170–186 K at 200 GPa. With a decrease in pressure, the T_c of Ca_8H_{46} increases to 210–223 K at 150 GPa, exceeding 200 K, which is the highest value among the

TABLE I. The calculated EPC parameter λ, logarithmic average phonon frequency ω_{log} (K), electronic density of states at Fermi level N (E_f) (states per eV), and superconducting transition temperatures T_c (K) of Ca_8H_{46}, Ca_8H_{45}, and Ca_8H_{44} with $\mu^* = 0.1$–0.13 at corresponding pressures.

	P (GPa)	λ	ω_{log}	N (E_f)	T_c (Allen-Dynes modified McMillan)	T_c (Eliashberg)
	200	1.53	1300.9	4.97	153–169	170–186
Ca_8H_{46}	170	2.04	1046.9	4.5	169–184	193–207
	150	3.16	699.9	4.73	171–187	210–223
	200	1.09	1352.9	2.58	98–114	107–122
Ca_8H_{45}	170	1.38	1150.5	2.66	119–133	131–145
	150	1.83	919.9	2.76	133–147	150–163
	200	0.51	1301.6	0.77	10–17	12–18
Ca_8H_{44}	170	0.59	1197.8	1.00	19–27	20–28
	150	0.73	1001.9	0.88	31–40	32–40

reported binary type-I clathrate hydrides. The T_c's of Ca_8H_{45} and Ca_8H_{44} are estimated to be 107–122 and 12–18 K at 200 GPa, respectively. For all structures, their ω_{log} values are around 1300 K at 200 GPa. Additionally, their λ and N (E_f) values change from 1.53 to 1.09 and further to 0.51, and 4.97 to 2.58 and further to 0.77 states per eV with the increase of hydrogen vacancies, and the T_c's decrease from 186 to 18 K, indicating that the T_c's are related with the λ and N (E_f). The calculated T_c's for Ca_8H_{46}, Ca_8H_{45}, and Ca_8H_{44}, with the experimentally measured T_c's for calcium hydrides, are shown in Fig. 4. The predicted T_c's of these hydrides gradually increase with decreasing pressure. However, the experimentally measured T_c's exhibit a sharp drop below 170 GPa upon decompression. Notably, the calculated T_c's for Ca_8H_{46} at 170 GPa and Ca_8H_{45} at 150 GPa are located in the experimental data range, which precisely corresponds to the experimental anomalies where T_c rapidly decreases upon decompression. Taking hydrogen vacancies into consideration offers insights into elucidating this anomalous phenomenon.

To gain deeper insights into the variations of the EPC, we plotted the phonon-dispersion curves, phonon density of states (PHDOS), Eliashberg spectral function α^2F (ω), and integral EPC parameter λ for Ca_8H_{46}, Ca_8H_{45}, and Ca_8H_{44} at 200, 170, and 150 GPa, as shown in Fig. 5 and Figs. S4–S6. There is no imaginary frequency indicating that they are dynamically stable at the corresponding pressures. In all structures, the phonon-dispersion curves can be distinctly divided into two regions: the low-frequency modes that are primarily attributed to the vibrations of the heavy Ca atoms, and the high-frequency modes that are predominantly due to the vibrations of the light H atoms. The integral curve of λ shows a rapid increase in the $750-1750\ cm^{-1}$ vibration range, aligning with the prominent peaks in the Eliashberg spectral function. It also reveals that the high-frequency modes contribute approximately 75–84% of the total EPC for all structures. For Ca_8H_{46}, there are noticeable soft phonon modes at the R point, which is beneficial for enhancing the EPC. For Ca_8H_{45}, and Ca_8H_{44}, the lack of soft phonon modes resulting in a decrease in λ from 1.53 (Ca_8H_{46}) to 1.09 (Ca_8H_{45}) and further to 0.51 (Ca_8H_{44}). Therefore, hydrogen vacancies significantly strengthen the hard phonon modes, leading to a marked decrease in the EPC of Ca_8H_{45} and Ca_8H_{44}.

The T_c's of Ca_8H_{45} and Ca_8H_{44} are significantly lower than that of Ca_8H_{46}. To clarify how the presence of hydrogen vacancies influences the variation in T_c's, we calculated their band structures and projected density of states (PDOS) at 200 GPa. The calculated band structures with PDOS are depicted in Fig. 6; bands crossing the Fermi level are annotated as numbers. For Ca_8H_{46}, two bands denoted as 1 and 2 cross the Fermi level. Band 1 exhibits a holelike band along the Brillouin zone's highly symmetric path M–Γ. Band 2 exhibits a flatband at the Fermi energy along path R–M and around the M point. Bands 1 and 2 meet along the Γ–R direction and exhibit a flatband just below the Fermi energy, giving rise to the presence of the Van Hove singularity (VHS) near the Fermi energy. For Ca_8H_{45} and Ca_8H_{44}, two and three bands cross the Fermi level, respectively. Different from Ca_8H_{46}, there is no flatband at or around Fermi level. The introduction of hydrogen vacancies moves the VHS away from the Fermi level, resulting in a decrease in the H PDOS at the Fermi level from 1.86 states per eV (Ca_8H_{46}) to 0.99 and 0.34 states per eV for Ca_8H_{45} and Ca_8H_{44}, respectively. A similar phenomenon appears in Li_2NaH_{17}. The vacancy structures $Li_2NaH_{16.5}$ and Li_2NaH_{16} also move the VHS away from the Fermi level, which reduces the content of H PDOS at the Fermi level [39]. The decrease in T_c for Ca_8H_{45} and Ca_8H_{44} is mainly attributed to the decrease in H PDOS and EPC.

For Ca_8H_{45} and Ca_8H_{44}, we calculated their enthalpy differences relative to Ca_8H_{46} (Figs. S7−S9). As the pressure decreases, Ca_8H_{45} and Ca_8H_{44} tend to exhibit greater stability than Ca_8H_{46} at 138 GPa, indicating that the ideal crystal could undergo dehydrogenation to form hydrogen-vacancy structures with a decrease in pressure. The transformation from the ideal crystal to hydrogen-vacancy structures as the pressure decreases could result in a decrease in T_c. Given that the unit cell of Ca_8H_{46} comprises 54 atoms, we calculated the T_c's of Ca_8H_{45} and Ca_8H_{44} with heavy hydrogen vacancies and did not consider the supercell with light hydrogen vacancy, which is computationally impossible. To assess the impact of hydrogen vacancies on the superconducting properties of Ca_8H_{46} by balancing the computational power and the number of hydrogen-vacancy candidate structures, we employed a $3 \times 1 \times 1$ supercell to generate hydrogen vacancies for calculating its PDOS. The calculated results show that the H PDOS

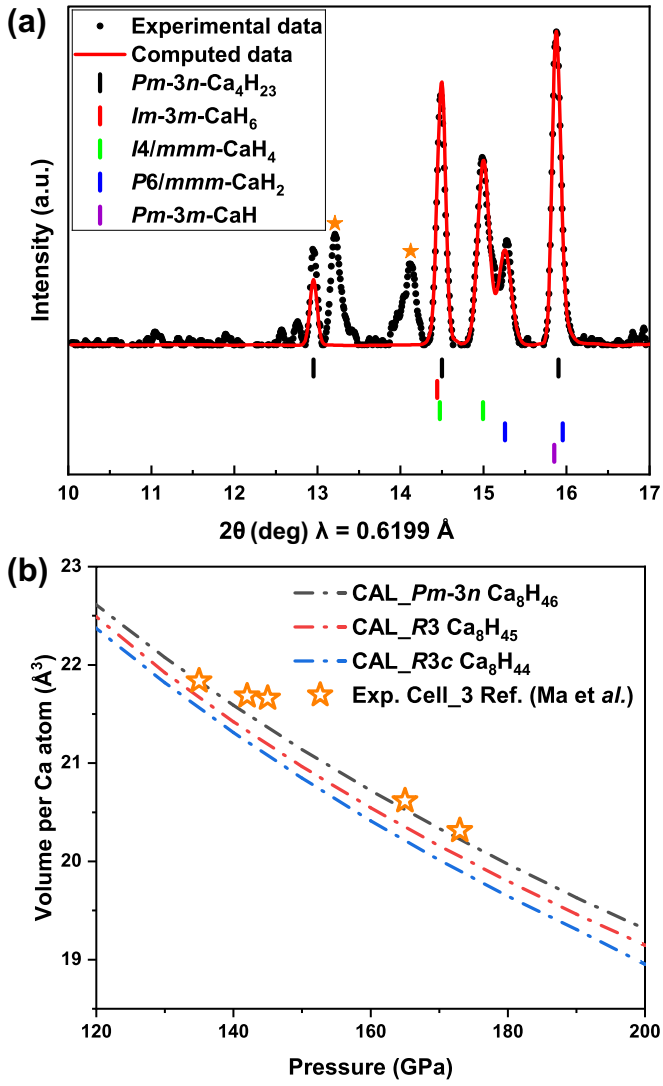

FIG. 3. (a) XRD patterns of calcium hydrides obtained from cell_3 reported by Ma *et al.* [13] and the refinement of predicted calcium hydride mixtures at 173 GPa. Black, red, green, blue, and purple tick marks represent the calculated peak positions of $Pm\bar{3}n$-Ca_8H_{46}, $Im\bar{3}m$-CaH_6, $I4/mmm$-CaH_4, $P6/mmm$-CaH_2, and $Pm\bar{3}m$-CaH, respectively. Unidentified peaks are indicated by orange solid stars. (b) Experimental EOS during decompression from cell_3 reported by Ma *et al.* [13] compared with predicted Ca_8H_{46}, Ca_8H_{45}, and Ca_8H_{44}. The black, red, and blue dashed lines represent the density-functional theoretically calculated volumes per Ca atom for Ca_8H_{46}, Ca_8H_{45}, and Ca_8H_{44}. The orange empty stars indicate the experimental EOS.

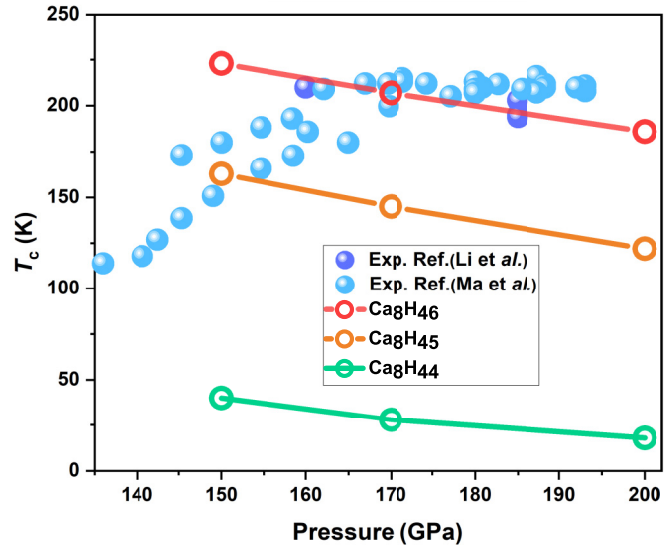

FIG. 4. Comparison between calculated T_c's of Ca_8H_{46}, Ca_8H_{45}, and Ca_8H_{44} and experimental data of calcium hydrides at corresponding pressures. Red, orange, and green hollow circles represent calculated T_c's of Ca_8H_{46}, Ca_8H_{45}, and Ca_8H_{44}, respectively. Blue and purple filled symbols represent measured T_c's from the literature [13,14].

values of $Ca_8H_{45.667}$ (also denoted as $Ca_{24}H_{137}$) and $Ca_8H_{45.333}$ (also denoted as $Ca_{24}H_{136}$) at the Fermi level are 2.11 and 1.26 states per eV. As hydrogen vacancies are introduced, the H PDOS values at the Fermi level first increase and then decrease (Fig. 7). For $Ca_8H_{45.667}$, the Fermi level shifts downward, reaching the VHS, and the H PDOS value increases (Fig. 7). Therefore, we speculate that T_c could be further enhanced at the optimal hydrogen vacancy. Considering the dependence of vacancy defects on T_c, we can estimate that the T_c of $Ca_8H_{45.333}$ lies between those of Ca_8H_{46} and Ca_8H_{45}.

The experimental measurement of the decrease in T_c's below 150 GPa is probably caused by Ca_8H_{45-x} $(0 < x < 1)$. These results suggest that the anomalous decrease in T_c observed in the experiment is attributable to the presence of hydrogen vacancies during decompression.

Notably, the synthesis of metastable hydride CaH_6 requires careful selection of precursors and control over the external environment that was achieved after a decade of exploration following its prediction. The key factor is precursor modification, transitioning from H_2 to NH_3BH_3 [13,14,20,21]. Recently, the synthesis of a thermodynamically metastable state Y_8H_{46} was induced by an x-ray free-electron laser, which drives nonequilibrium processes [40]. Thermodynamically metastable hydride syntheses are influenced by precursor modification and experimental conditions. Compared with thermodynamically metastable structures, the synthesis conditions for thermodynamically stable structures are less stringent. For YH_6, which is isomorphic to CaH_6, successful synthesis can be achieved by compressing Y in H_2, YH_3 in H_2, Y with NH_3BH_3, and YH_3 with NH_3BH_3 [12]. CeH_9 can be synthesized by cooling compression without the need for laser heating [41,42]. Therefore, it is highly likely that the thermodynamically stable structure Ca_8H_{46} and its hydrogen-vacancy structures have probably appeared in previous experiments [13,14].

IV. CONCLUSION

A thermodynamically stable type-I clathrate hydride, $Pm\bar{3}n$-Ca_8H_{46}, was shown by an extensive structure search at 200 GPa. It exhibits a T_c of 223 K at 150 GPa, marking the highest T_c observed among predicted and synthesized binary type-I clathrate hydrides. The simulated XRD patterns and calculated EOS results demonstrate a good agreement

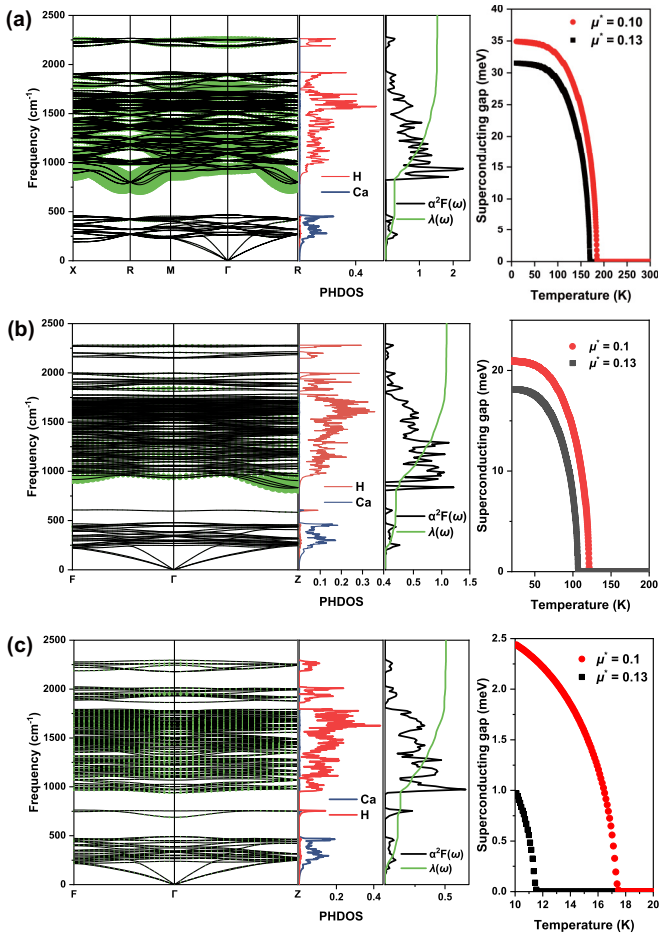

FIG. 5. Phonon-dispersion curves (left), phonon density of states (PHDOS), Eliashberg spectral function α^2F (ω), and EPC parameter $\lambda(\omega)$ (middle), and superconducting gap (right) of (a) Ca_8H_{46}, (b) Ca_8H_{45}, and (c) Ca_8H_{44} at 200 GPa. The size of green dots on phonon-dispersion curves means the magnitudes of phonon linewidth.

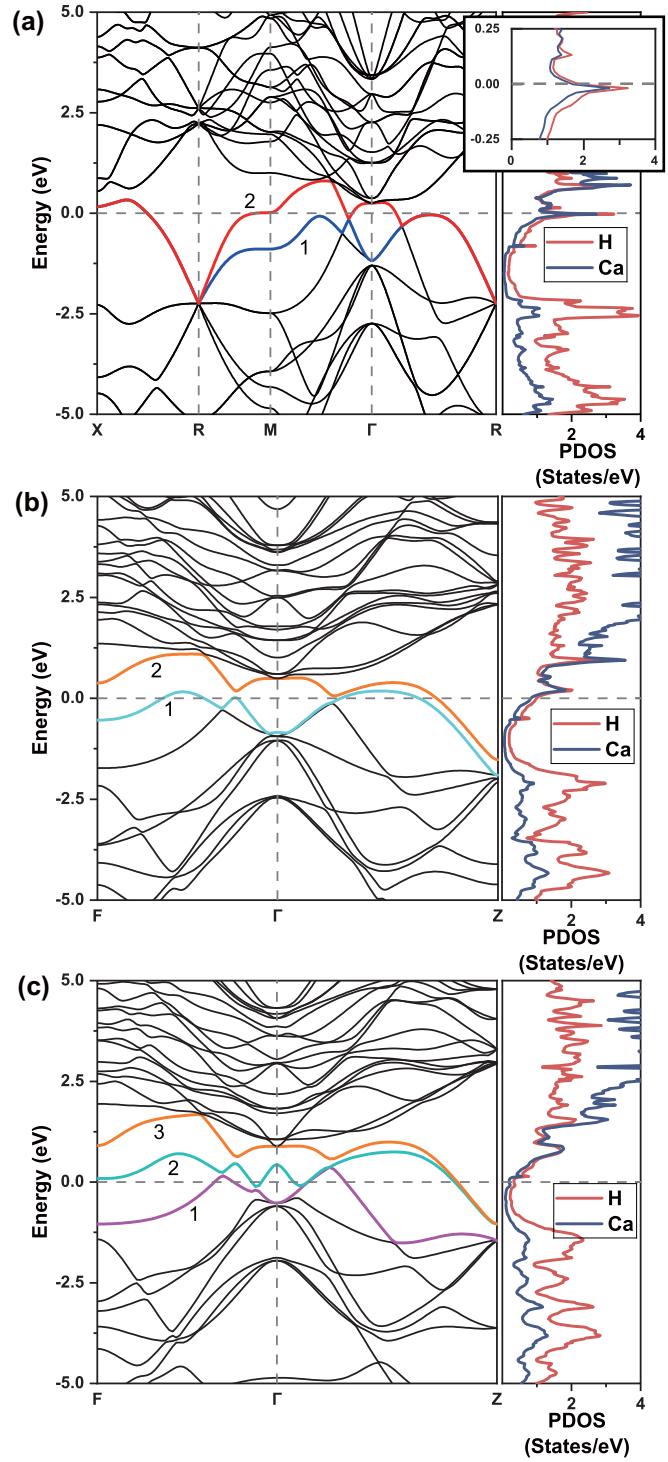

FIG. 6. Calculated band structures and PDOS of (a) Ca_8H_{46}, (b) Ca_8H_{45}, and (c) Ca_8H_{44} at 200 GPa. A detailed view of the PDOS near the VHS of Ca_8H_{46} is provided in the inset of (a).

with experimental measurements, confirming the successful synthesis of Ca_8H_{46}. The introduction of hydrogen vacancies in Ca_8H_{46} induces structural distortion and a significant variation in T_c, explaining the abnormal drop in T_c observed in experiments. Further analysis shows that the type-I clathrate hydride and its hydrogen-vacancy structures are likely to be commonly present in the high-pressure synthesis of alkaline- and rare-earth metal hydrides. The synthesis of hydrides under high pressure strongly depends on precursors and external conditions, thereby requiring the collaboration of theoretical and experimental researchers to explore the mechanisms for achieving precise control of high-temperature superconducting hydride synthesis.

ACKNOWLEDGMENTS

We are grateful to H. B. Wang and X. C. Wang for the experimental data and discussion. This work was supported by the National Natural Science Foundation of China (Grants No. 12122405, No. 52072188, and No. 12274169), the National Key Research and Development Program of China (Grant No. 2022YFA1402304), the Program for Science and Technology Innovation Team in Zhejiang (Grant No. 2021R01004), and the Fundamental Research Funds for the Central Universities. Some of the calculations were performed at the High Performance Computing Center of Jilin University and using TianHe-1(A) at the National Supercomputer Center in Tianjin.

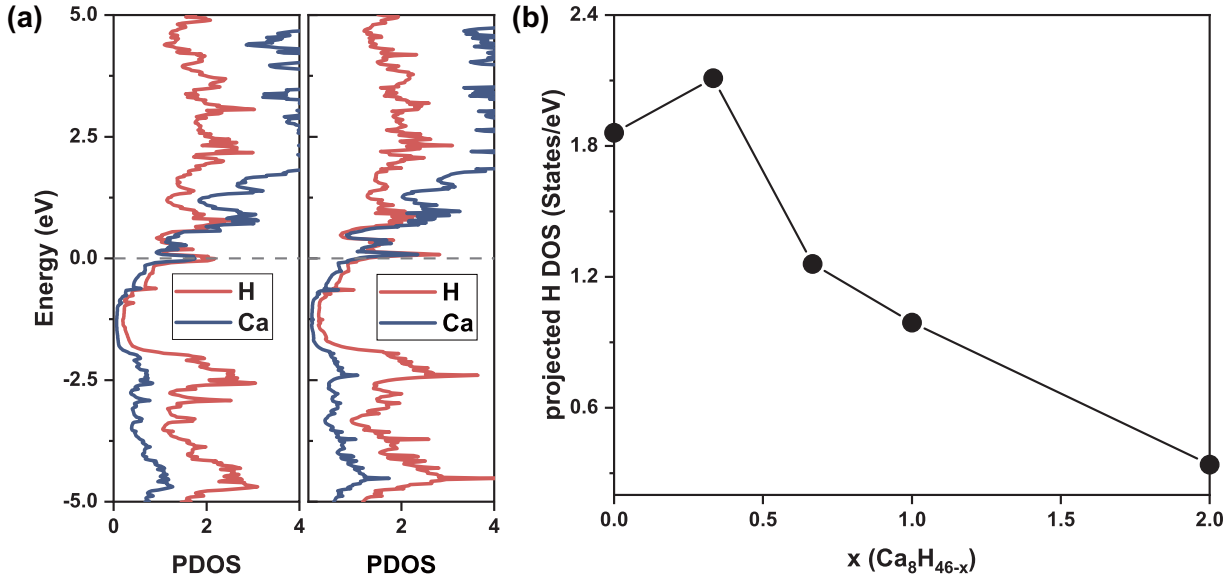

FIG. 7. Calculated projected DOS of (a) $Ca_8H_{45.667}$ and $Ca_8H_{45.333}$ at 200 GPa. (b) The projected H DOS value of Ca_8H_{46-x} ($x = 0$, 0.333, 0.667, 1, and 2) at 200 GPa.

[1] D. Duan, Y. Liu, F. Tian, D. Li, X. Huang, Z. Zhao, H. Yu, B. Liu, W. Tian, and T. Cui, Pressure-induced metallization of dense $(H_2S)_2H_2$ with high-T_c superconductivity, Sci. Rep. **4**, 6968 (2015).

[2] Y. Li, J. Hao, H. Liu, Y. Li, and Y. Ma, The metallization and superconductivity of dense hydrogen sulfide, J. Chem. Phys. **140**, 174712 (2014).

[3] A. P. Drozdov, M. I. Eremets, I. A. Troyan, V. Ksenofontov, and S. I. Shylin, Conventional superconductivity at 203 Kelvin at high pressures in the sulfur hydride system, Nature (London) **525**, 73 (2015).

[4] W. Zhao, X. Huang, Z. Zhang, S. Chen, M. Du, D. Duan, and T. Cui, Superconducting ternary hydrides: Progress and challenges, Natl. Sci. Rev. **11**, nwad307 (2024).

[5] L. Zhu, H. Liu, M. Somayazulu, Y. Meng, P. A. Guńka, T. B. Shiell, C. Kenney-Benson, S. Chariton, V. B. Prakapenka, H. Yoon, J. A. Horn, J. Paglione, R. Hoffmann, R. E. Cohen, and T. A. Strobel, Superconductivity in SrB_3C_3 clathrate, Phys. Rev. Res. **5**, 013012 (2023).

[6] Z. Guo, X. Li, A. Bergara, S. Ding, X. Zhang, and G. Yang, Pressure-induced evolution of stoichiometries and electronic structures of host–guest Na–B compounds, Matter Radiat. Extremes **8**, 068401 (2023).

[7] H. Xie, H. Wang, F. Qin, W. Han, S. Wang, Y. Wang, F. Tian, and D. Duan, A fresh class of superconducting and hard pentaborides, Matter Radiat. Extremes **8**, 058404 (2023).

[8] H. Liu, I. I. Naumov, R. Hoffmann, N. W. Ashcroft, and R. J. Hemley, Potential high- T_c superconducting lanthanum and yttrium hydrides at high pressure, Proc. Natl. Acad. Sci. USA **114**, 6990 (2017).

[9] F. Peng, Y. Sun, C. J. Pickard, R. J. Needs, Q. Wu, and Y. Ma, Hydrogen clathrate structures in rare earth hydrides at high pressures: Possible route to room-temperature superconductivity, Phys. Rev. Lett. **119**, 107001 (2017).

[10] H. Wang, J. S. Tse, K. Tanaka, T. Iitaka, and Y. Ma, Superconductive sodalite-like clathrate calcium hydride at high pressures, Proc. Natl. Acad. Sci. USA **109**, 6463 (2012).

[11] A. P. Drozdov, P. P. Kong, V. S. Minkov, S. P. Besedin, M. A. Kuzovnikov, S. Mozaffari, L. Balicas, F. F. Balakirev, D. E. Graf, V. B. Prakapenka, E. Greenberg, D. A. Knyazev, M. Tkacz, and M. I. Eremets, Superconductivity at 250 K in lanthanum hydride under high pressures, Nature (London) **569**, 528 (2019).

[12] P. Kong, V. S. Minkov, M. A. Kuzovnikov, A. P. Drozdov, S. P. Besedin, S. Mozaffari, L. Balicas, F. F. Balakirev, V. B. Prakapenka, S. Chariton, D. A. Knyazev, E. Greenberg, and M. I. Eremets, Superconductivity up to 243 K in the yttrium-hydrogen system under high pressure, Nat. Commun. **12**, 5075 (2021).

[13] L. Ma, K. Wang, Y. Xie, X. Yang, Y. Wang, M. Zhou, H. Liu, X. Yu, Y. Zhao, H. Wang, G. Liu, and Y. Ma, High-Temperature superconducting phase in clathrate calcium hydride CaH_6 up to 215 K at a pressure of 172 GPa, Phys. Rev. Lett. **128**, 167001 (2022).

[14] Z. Li, X. He, C. Zhang, X. Wang, S. Zhang, Y. Jia, S. Feng, K. Lu, J. Zhao, J. Zhang, B. Min, Y. Long, R. Yu, L. Wang, M. Ye, Z. Zhang, V. Prakapenka, S. Chariton, P. A. Ginsberg, J. Bass, S. Yuan, H. Liu, and C. Jin, Superconductivity above 200 K discovered in superhydrides of calcium, Nat. Commun. **13**, 2863 (2022).

[15] D. Laniel, F. Trybel, B. Winkler, F. Knoop, T. Fedotenko, S. Khandarkhaeva, A. Aslandukova, T. Meier, S. Chariton, K. Glazyrin, V. Milman, V. Prakapenka, I. A. Abrikosov, L. Dubrovinsky, and N. Dubrovinskaia, High-pressure synthesis of seven lanthanum hydrides with a significant variability of hydrogen content, Nat. Commun. **13**, 6987 (2022).

[16] Y. Li, B. Li, T. Cui, Y. Li, L. Zhang, Y. Ma, and G. Zou, High-pressure phase transformations

in CaH_2, J. Phys.: Condens. Matter **20**, 045211 (2008).

[17] Z. Shao, D. Duan, Y. Ma, H. Yu, H. Song, H. Xie, D. Li, F. Tian, B. Liu, and T. Cui, Unique phase diagram and superconductivity of calcium hydrides at high pressures, Inorg. Chem. **58**, 2558 (2019).

[18] Y. Chen, Z. Liu, Z. Lin, Q. Jiang, M. Du, Z. Zhang, H. Song, H. Xie, T. Cui, and D. Duan, High T_c superconductivity in layered hydrides XH_{15} (X = Ca, Sr, Y, La) under high pressures, Front. Phys. **17**, 63502 (2022).

[19] Q. Wang, S. Zhang, H. Li, H. Wang, G. Liu, J. Ma, H. Xu, H. Liu, and Y. Ma, Coexistence of superconductivity and electride states in Ca_2H with an antifluorite-type motif under compression, J. Mater. Chem. A **11**, 21345 (2023).

[20] A. K. Mishra, T. Muramatsu, H. Liu, Z. M. Geballe, M. Somayazulu, M. Ahart, M. Baldini, Y. Meng, E. Zurek, and R. J. Hemley, New calcium hydrides with mixed atomic and molecular hydrogen, J. Phys. Chem. C **122**, 19370 (2018).

[21] G. Wu, X. Huang, H. Xie, X. Li, M. Liu, Y. Liang, Y. Huang, D. Duan, F. Li, B. Liu, and T. Cui, Unexpected calcium polyhydride CaH_4: A possible route to dissociation of hydrogen molecules, J. Chem. Phys. **150**, 044507 (2019).

[22] C. J. Pickard and R. J. Needs, *Ab initio* random structure searching, J. Phys.: Condens. Matter **23**, 053201 (2011).

[23] G. Kresse and J. Furthmüller, Efficiency of *ab-initio* total energy calculations for metals and semiconductors using a plane-wave basis set, Comput. Mater. Sci. **6**, 15 (1996).

[24] J. P. Perdew, K. Burke, and M. Ernzerhof, Generalized gradient approximation made simple, Phys. Rev. Lett. **77**, 3865 (1996).

[25] B. H. Toby, *EXPGUI*, a graphical user interface for *GSAS*, J. Appl. Cryst. **34**, 210 (2001).

[26] P. Giannozzi *et al.*, QUANTUM ESPRESSO: A modular and open-source software project for quantum simulations of materials, J. Phys.: Condens. Matter **21**, 395502 (2009).

[27] D. Vanderbilt, Soft self-consistent pseudopotentials in a generalized eigenvalue formalism, Phys. Rev. B **41**, 7892 (1990).

[28] P. B. Allen and R. C. Dynes, Transition temperature of strong-coupled superconductors reanalyzed, Phys. Rev. B **12**, 905 (1975).

[29] G. M. Eliashberg, Interactions between electrons and lattice vibrations in a superconductor, JETP **11**, 696 (1960).

[30] E. R. Margine and F. Giustino, Anisotropic Migdal-Eliashberg theory using Wannier functions, Phys. Rev. B **87**, 024505 (2013).

[31] A. Sanna, J. A. Flores-Livas, A. Davydov, G. Profeta, K. Dewhurst, S. Sharma, and E. K. U. Gross, *Ab initio* Eliashberg theory: Making genuine predictions of superconducting features, J. Phys. Soc. Jpn. **87**, 041012 (2018).

[32] See Supplemental Material at http://link.aps.org/supplemental/10.1103/PhysRevB.110.054505 for convex hull, x-ray-diffraction patterns, phonon dispersions, vacancy formation enthalpy, and structure information.

[33] Y. Sun and M. Miao, Assemble superhydrides with non-integer H/Metal ratios on metal templates, arXiv:2303.05721.

[34] Y. Sun and M. Miao, Chemical templates that assemble the metal superhydrides, Chem **9**, 443 (2023).

[35] S. Arapan, H. Mao, and R. Ahuja, Prediction of incommensurate crystal structure in Ca at high pressure, Proc. Natl. Acad. Sci. USA **105**, 20627 (2008).

[36] C. J. Pickard and R. J. Needs, Structure of phase III of solid hydrogen, Nat. Phys. **3**, 473 (2007).

[37] J. S. Kasper, P. Hagenmuller, M. Pouchard, and C. Cros, Clathrate structure of silicon Na_8Si_{46} and Na_xSi_{136} ($x < 11$), Science **150**, 1713 (1965).

[38] F. C. Frank and J. S. Kasper, Complex alloy structures regarded as sphere packings. I. Definitions and basic principles, Acta Cryst. **11**, 184 (1958).

[39] D. An, D. Duan, Z. Zhang, Q. Jiang, H. Song, and T. Cui, Thermodynamically stable room-temperature superconductors in Li-Na hydrides under high pressures, arXiv:2303.09805.

[40] E. Siska *et al.*, Ultra-fast yttrium hydride chemistry at high pressures via non-equilibrium states induced by x-ray free electron laser, arXiv:2307.11293.

[41] X. Li, X. Huang, D. Duan, C. J. Pickard, D. Zhou, H. Xie, Q. Zhuang, Y. Huang, Q. Zhou, B. Liu, and T. Cui, Polyhydride CeH9 with an atomic-like hydrogen clathrate structure, Nat. Commun. **10**, 3461 (2019).

[42] W. Chen, D. V. Semenok, X. Huang, H. Shu, X. Li, D. Duan, T. Cui, and A. R. Oganov, High-Temperature superconducting phases in cerium superhydride with a T c up to 115 K below a pressure of 1 megabar, Phys. Rev. Lett. **127**, 117001 (2021).